

Case History

Traveltime tomography of a dense wide-angle profile across Orphan Basin

Louise Watremez¹, K. W. Helen Lau², Mladen R. Nedimović³, and Keith E. Louden²

ABSTRACT

We used first arrivals and Moho reflections from the 500-km-long Orphan Basin Wide-Angle Velocity Experiment (OB-WAVE) profile with 3–5-km instrument spacing to construct a traveltimes tomography section and to delineate the Moho discontinuity across the Orphan Basin. The Orphan Basin is a failed rift located offshore Newfoundland, Canada, showing thinned continental crust over an unusually wide region. We observed (1) a zone of extreme crustal thinning (<7-km-thick crust) with no evidence for mantle serpentinization, (2) basement morphology exhibiting tilted blocks linked to the crustal thinning, and (3) a thicker central crustal segment that is probably related to prerift structural inheritance. Comparison with the adjacent Jeanne d'Arc Basin to the southeast suggested the

presence of a decoupling zone between the two basins accommodating the difference in extension rates. There was a good correlation between the tomographic velocities and the reflection structure derived from a coincident seismic reflection profile except in an area in which the reflection seismic data suggested the presence of a deep sedimentary basin. The velocity model computed in this work indicated that this area consists of prerift basement rather than Jurassic or older sediments. Tomographic models computed by varying the density of the recording instrument array gave insight into the relationship among the target size, the instrument spacing needed to resolve it, and the velocity model uncertainty. These results may help guide the design of future wide-angle reflection and refraction surveys across rifted structures.

INTRODUCTION

Continental extension is a process governed by a broad range of parameters that control the mechanical properties of the lithosphere. These parameters, for example, include the thermal state of the lithosphere, the presence of prerift-inherited structures in the crust, and the far-field forces (e.g., Kuszniir and Park, 1987; Buck, 1991; Karner et al., 1993; Burrov and Diament, 1995; Huismans and Beaumont, 2011). Knowledge about the rifted structures at all stages of rifting, from the beginning of continental extension to continental breakup, is necessary to fully understand the processes

of continental rifting and, ultimately, breakup. Therefore, rifted structures are widely studied at different stages of the evolution of the rift, from the beginning of continental extension, as found at the Baikal rift, to continental breakup, such as the North Atlantic rifted margins (e.g., Petit and Déverchère, 2006; Thybo and Nielsen, 2009; Lundin and Doré, 2011).

Here, we present a refraction and wide-angle reflection study of the Orphan Basin, which is located on the northeast margin of eastern Canada (Figure 1) and is of great interest for academic and industry investigators. Previous studies have shown that Orphan Basin represents a wide zone of extended continental crust, with an

Manuscript received by the Editor 12 August 2014; revised manuscript received 22 December 2014; published online 3 April 2015.

¹Formerly Dalhousie University, Department of Oceanography, Halifax, Nova Scotia, Canada; presently University of Southampton, National Oceanography Centre, Southampton, UK. E-mail: louise.watremez@dal.ca.

²Dalhousie University, Department of Oceanography, Halifax, Nova Scotia, Canada. E-mail: kwhlau@dal.ca; keith.louden@dal.ca.

³Dalhousie University, Department of Earth Sciences, Halifax, Nova Scotia, Canada. E-mail: mladen@dal.ca.

© 2015 Society of Exploration Geophysicists. All rights reserved.

average β of approximately 2, thus allowing us to study both the early and middle stages of continental extension (e.g., Keen and Dehler, 1993; Chian et al., 2001). The stretching factor β is a measure of the total strain resulting from the extension (McKenzie, 1978). The possibility to study the early and middle stages of extension is particularly attractive because these stages are generally not well documented on continental margins in which the crust often thins rapidly before reaching a highly extended transition region of complex crustal type (e.g., Reston, 2009).

Although top sections of complex rifted structures have been identified in the Orphan Basin based on detailed grids of seismic reflection profiles (e.g., Enachescu et al., 2005), it has not yet been possible to connect these structures with images of deep crustal variations from refraction studies with sufficiently high resolution. For example, only 15 ocean-bottom seismometers (OBSs) were used

along a 350-km-long refraction profile in the study of Chian et al. (2001) across the Orphan Basin, and due to the low-resolving power of this sparsely instrumented profile, there appears to be little relationship between large-scale basement relief and variations in the deep crust. Evidence for extreme crustal thinning has also been identified across the Orphan Basin using 3D gravity modeling, with some thickness estimates at some locations being as little as 5 km (Welford and Hall, 2007), but such models lack support from clear images of deep crustal structures on wide-angle seismic profiles.

In 2010, supported by ExxonMobil, we undertook the Orphan Basin Wide-Angle Velocity Experiment (OBWAVE) survey to provide detailed crustal-scale refraction and wide-angle reflection constraints along a 500-km-long dense OBS profile across the Orphan Basin. The strike of the profile is parallel to the average direction of rifting (Sibuet et al., 2007). We use joint tomography inversion of the first arrivals and wide-angle arrivals from phases reflected on the Moho to determine the crustal and upper-mantle velocities, as well as the depth to the Moho.

Significantly smaller instrument spacing (3–5 km) than that used for standard refraction and wide-angle reflection surveys (10–25 km, e.g., Funck et al., 2003, 2004; Contrucci et al., 2004; Klingelhoefer et al., 2009) allows us to perform an analysis of the impact of instrument spacing on the image resolution, which is an important factor for survey design. A coincident seismic reflection profile acquired by Geophysical Service Incorporated (line Or0-122) and interpreted by others (e.g., Enachescu et al., 2005) is used in this work and used for independent comparison and joint interpretation. At the most regional scale, our results provide new insight into the relationship between the Orphan Basin and the Jeanne d'Arc Basin. At a much smaller scale, our results shed new light on the distribution of Mesozoic subbasins.

GEOLOGIC SETTING

Orphan Basin is located offshore Newfoundland, north of the Grand Banks and Jeanne d'Arc Basin, and west of the Flemish Cap. It formed during multiple episodes of rifting beginning at or before the late Triassic and ending in the late Aptian, based on age constraints from deep-water wells (e.g., the Blue, Great-Barasway, and Lona wells; Ford and Johnston, 2003). The basin contains multiple faults that are interpreted to terminate in the midcrust (de Voogd and Keen, 1987; Bassi et al., 1993; Chian et al., 2001). However, existing seismic reflection profiles do not provide good constraints on the depth of the basement and Moho, primarily because Moho reflections are often not well imaged. Chian et al. (2001) use gravity modeling to show that continental crust almost broke apart beneath the Bonavista Platform, with crust thicknesses of less than 5 km. They observe

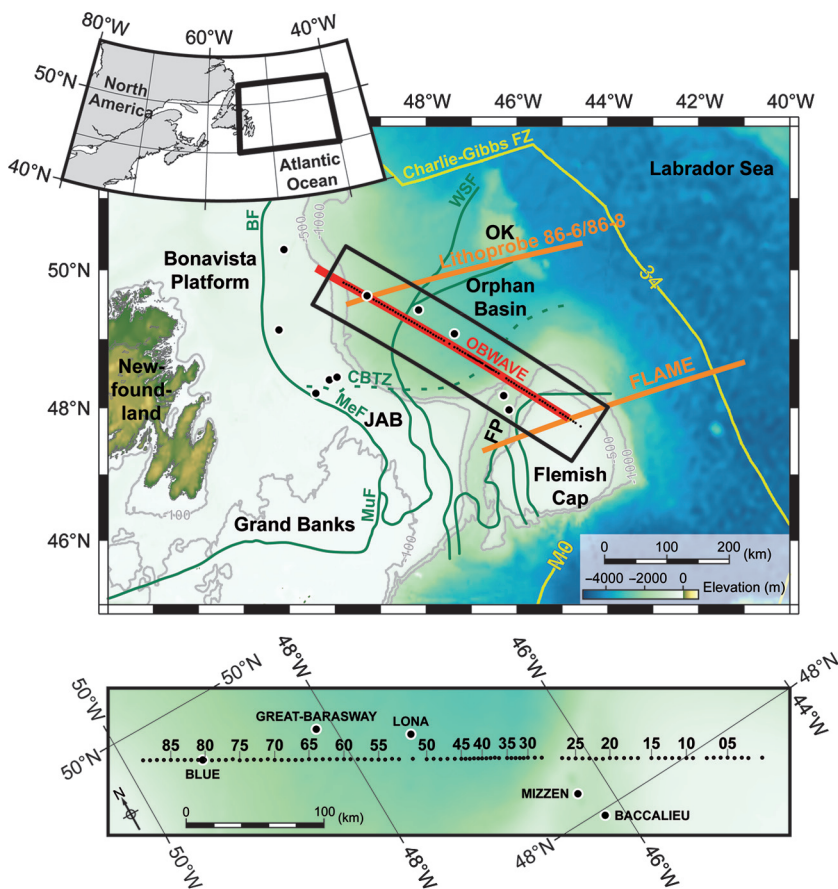


Figure 1. (a) Location of the OBWAVE profile superimposed on a bathymetric map of the study area (data are from Ryan et al., 2009). The red line shows the position of the OBWAVE shot line, and the black dots are positions of the OBS along the line. Two orange lines show the positions of two published refraction lines (Chian et al. [2001], Lithoprobe 86-6/86-8 profile; and Gerlings et al. [2011], FLAME profile). Black circles bordered by white show the positions of Orphan Basin boreholes. The yellow lines show the position of the initial seafloor magnetic anomalies (from Müller et al., 1997), and the green lines show the position of the main tectonic features (from Enachescu et al., 2004). The black rectangle indicates the position of the map at the bottom of the figure. BF, Bonavista Fault; CBTZ, Cumberland Belt Transfer Zone; FP, Flemish Pass; JAB, Jeanne d'Arc Basin; OK, Orphan Knoll; MeF, Mercury Fault; MuF, Murre Fault; and WSF, White Sail Fault. The map inset (top left) shows the location of the study area (black rectangle) relative to eastern North America. (b) Magnification of the main map showing position and numbering of the instruments along the line and nearby boreholes with their names. The color scale for the bathymetry is the same as in the main map.

no magmatic underplating, showing that the rifting process was primarily nonvolcanic.

The Orphan Basin terminates to the south against the petroliferous Jeanne d'Arc Basin, which is separated from it by the Cumberland Belt Transfer Zone. This transfer zone is interpreted as a decoupling zone between the Orphan Basin and the Jeanne d'Arc Basin during the rifting (Figure 1, Skogseid, 2010; Lundin and Doré, 2011). The Jeanne d'Arc and Flemish Pass basins were also affected by several episodes of rifting, similar to the Orphan Basin (e.g., Enachescu et al., 2005; Sibuet et al., 2007; Baur et al. 2010). From the point of view of recent exploration significance, a major petroleum deposit (Bay du Nord) was drilled in the Flemish Pass Basin. This is only 40 km south of the Mizzen borehole (Figure 1) that, together with Harpoon, is also a recent petroleum discovery by Statoil.

DATA ACQUISITION AND PROCESSING

Orphan Basin Wide-Angle Velocity Experiment

The OBWAVE survey was conducted offshore Newfoundland in September-October 2010 onboard the R/V *Strait Explorer*. The experiment used 31 instruments from the U.K. Ocean-Bottom Instrumentation Consortium (OBIC) and 21 instruments from Dalhousie University and the Geological Survey of Canada. The OBSs were deployed twice to acquire a 500-km-long refraction line with instrument spacing of 3–5 km. A total of 100 instruments were deployed. Three instruments were lost, four instruments did not acquire a readable signal, and four instruments were double deployments for tests. Thus, 89 OBS recordings were available for analysis (Figure 1). The sample rate of the data is 4 ms, and recordings included data from hydrophone and 3C geophone sensors.

The acoustic source consisted of an array of nine ~ 8.4 L (512 in³) G-guns giving a total volume of 75.5 L (4608 in³). The OBS recorded a total of 6780 shots during the experiment: 2032 shots during the first deployment and 4748 shots during the second deployment, which included double coverage by shooting in both profile directions to improve shot density during rough seas. Shots were triggered every 60 s at a ship speed of 4–5 knots, giving an average shot spacing of approximately 140 m. Instruments were relocated on the seafloor using the measured sound speed profile in the water column, the water depth from an echo sounder, and the OBS direct-wave arrival times. OBS spacing is 5 km for model distances from 45 to 275 km and 330 to 500 km, and 3 km from 275 to 330 km. Shots were triggered at model distances from 0 to 470 km.

Wrap-around noise removal

The acquired data were generally of very good quality, allowing us to identify reflected and refracted arrivals out to offsets of 80–100 km on many instruments. However, the 60-s interval between shots resulted in wrap-around noise (i.e., the direct wave from the previous shot arriving at the same time as ground waves of interest) for offsets of 80 to 130 km (Figure 2a and 2b, top panels). The wrap-around noise shows apparent velocities from 1500 m/s (water velocity) to up to 4300 m/s (unconsolidated sediments), has strong amplitudes and is much slower than crustal and mantle phases, which are the phases of interest. This broadband high-amplitude

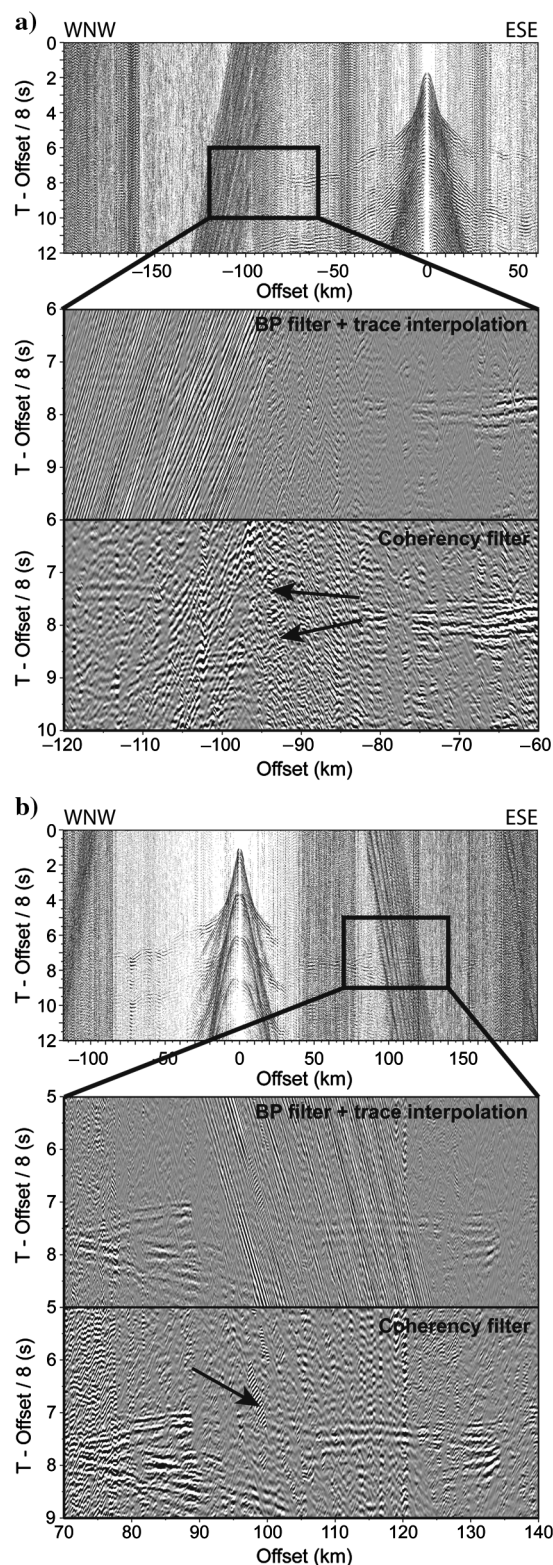


Figure 2. Examples of OBS receiver gathers (a) 44 and (b) 75 before and after wrap-around noise removal. (a) The close-up view shows areas in which arrivals of interest are masked by the wrap-around noise. Panels (a and b) show the data after band-pass filtering and trace interpolation. Panel (b) shows the data after coherency filtering. The black arrows point to additional arrivals of interest that have been picked after removal of wrap-around noise.

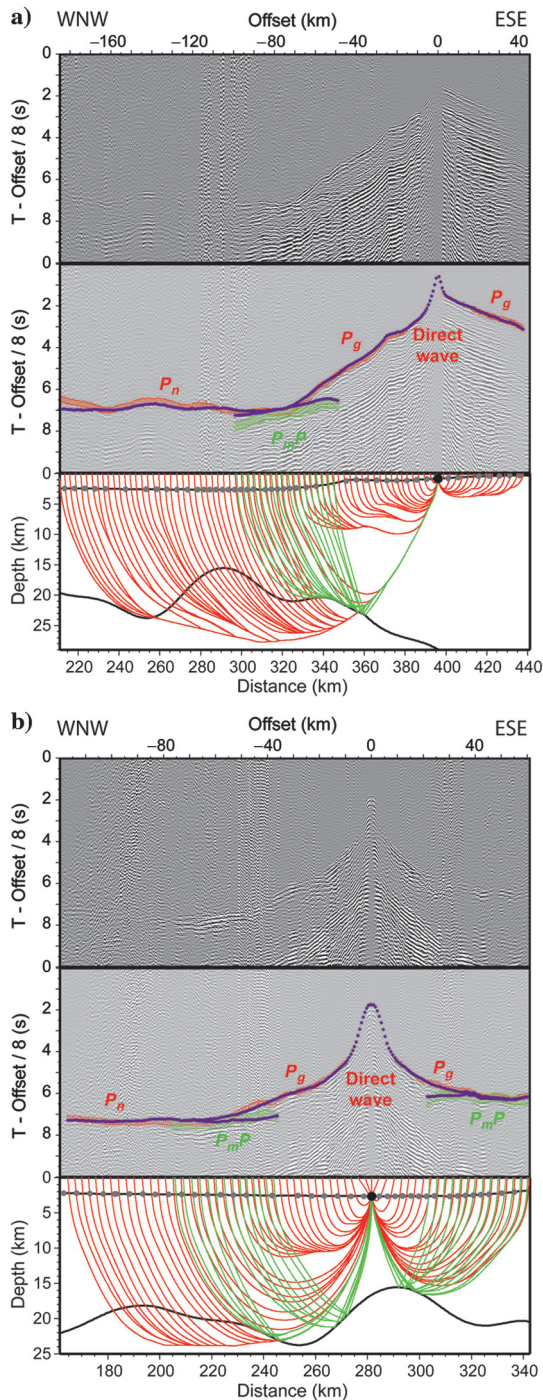


Figure 3. Examples of OBS sections with wrap-around noise removal applied (top panels), picked arrival times (center panels), and ray tracing in the model (lower panels) for (a) OBS 18 vertical geophone and (b) OBS 44 vertical geophone. Data are shown with a reduction velocity of 8 km/s. The picked arrival times are shown in red for the first arrivals of phases refracted in the crust and mantle P_g and P_n and green for the wide-angle reflections from the Moho P_mP . The heights of the picks correspond to their uncertainties. The purple dots are calculated arrival times after ray tracing in the final velocity model. The red rays are the refracted rays corresponding to the first-arrival picks, and the green rays are the wide-angle reflections from the modeled Moho (black line). Every twentieth ray is shown. The gray circles show the positions of the OBS on the seafloor, and the larger black circles identify the particular OBS in the examples.

steeply dipping noise masks ground-wave arrivals with much lower amplitude and dip.

To remove most of this noise, we apply a wrap-around noise removal process. We first sort the data into receiver gathers (e.g., hydrophone or vertical geophone components) with the traces ordered by shot number or source-receiver offset, and we use an amplitude spike removal to suppress energy bursts. Median amplitudes, which are used to set the acceptable amplitude window for the data, are calculated by computing root-mean-square (rms) values in a sliding window that is 11 traces wide and 200 ms high. To prevent aliasing during application of a local $f-k$ coherency filter, data are band-pass filtered and interpolated (Figure 2a and 2b, middle panels). The corner frequencies of the minimum phase trapezoidal band-pass filter applied are 1–3–12–18 Hz. Trace interpolation parameters are 30 m trace spacing, 1 km spatial gate, 1 ms/m maximum dip, and 400 ms coherency smoothing wavelet length. The local $f-k$ coherency filter is 1020 m (35 traces) wide and 120 ms (31 samples) long, with a dip pass range of -7 to 7 ms/trace. This dip range preserves higher phase velocity arrivals of interest and removes arrivals with apparent velocities of <4.3 km/s, for water and sediment arrivals (bottom panels of Figure 2a and 2b). This described filter process is used only for picking of large offset arrivals. Figure 2 shows two examples of data in which the wrap-around noise removal significantly improved the identification of far-offset arrivals. For low-velocity arrivals, the applied filtering degrades the signal and has to be used with care during picking.

Data picking

First-arrival times of refracted waves (e.g., P_g and P_n , Figure 3), and later reflected arrival times from the Moho (P_mP) were hand picked on unfiltered, vertical geophone data or, if the geophone data were not of sufficient quality, band-pass filtered hydrophone data. Additional traveltimes were added using the coherency-filtered data set (Figure 3), increasing the total number of picks by 10%. These far-offsets picks (>80 km) correspond to raypaths that sample the deepest parts of the crust and upper mantle. A total of 81,049 first arrival times and 26,174 P_mP arrival times were picked. Picking uncertainties of the refracted arrivals were defined using the signal-to-noise ratio (S/N) of the seismic data, by comparing the amplitudes 200 ms before and 200 ms after the pick, following the parameterization of Zelt and Forsyth (1994). Uncertainties for first-arrival times range from 20 to 125 ms, depending on the S/N. Average uncertainty for the picks of first arrival times is of 101 ms. The picking uncertainty of the P_mP arrivals was set to 200 ms because P_mP corresponds to a complex set of arrivals on many instruments, implying that the Moho is probably not a sharp interface in some areas of the basin but rather a complex transition zone (Figure 3).

Traveltime tomography

The P-wave traveltime tomography was carried out using TOMO2D (Korenaga et al., 2000). TOMO2D allows for joint tomography inversion of refracted first-arrival traveltimes and later reflection arrivals arising from a single interface (in our case, the Moho) in a sheared mesh model, hanging from the seafloor. Cells are parallelograms with the top and bottom sides parallel to the seafloor and the two other sides being vertical (see Korenaga et al. [2000] for more details). Cells in our model are 500-m wide, and their height varies from 100 m at the seafloor to 500 m at

the bottom of the model, 50 km beneath the seafloor, with the cell heights linearly increasing with depth. The Moho is modeled as a floating reflector with depth nodes every 500 m.

Traveltime tomography using Tomo2D produces a smooth velocity model using minimum a priori information. This means that there are no velocity discontinuities anywhere in the model, including the Moho. Although, tomography can include velocity discontinuities, in this work, we choose to avoid this approach because it requires additional user input, which can be subjective and may not be necessary considering the close OBS spacing at which data were collected.

The tomography is carried out in two steps: (1) ray tracing (i.e., forward problem) and (2) the linearized inversion (i.e., inverse problem). The forward problem consists of finding the shortest raypath from the shot to the receiver for each arrival time following a hybrid approach that combines graph and ray-bending methods (Moser, 1991; Moser et al., 1992; Van Avendonk et al., 1998; Korenaga et al., 2000). We use a tenth-order forward star (Zhang and Toksöz, 1998) for the graph method and a minimum segment length of 1 km with 10 interpolation points per segment for the bending method (Papazachos and Nolet, 1997). Tolerances are 5×10^{-4} s and 5×10^{-5} s for the conjugate gradient and Brent minimization, respectively.

Tomography inversion results in a reduction in the residuals between picked and calculated traveltimes through model updates by perturbation of velocities and depth of the interface nodes, using a least-squares regularized inversion (see Korenaga et al. [2000] for more details). Parameters for the inversion were chosen, similar to the forward problem, after a full parametric study. The correlation lengths control the smoothness of the model perturbations (i.e., the inversion stability). For the velocity nodes, we use horizontal correlation lengths that linearly increase from 3 to 30 km from the seafloor to the base of the model and vertical correlation lengths that linearly increase from 1 to 10 km from the seafloor to the base of the model. The correlation length for the depth of the interface nodes is set to 6 km. Weighting parameters also control the smoothing and the damping constraints. The depth kernel weighting parameter is equal to 0.1, to favor stronger velocity perturbations relative to the interface depth perturbations. Indeed, we favor strong velocity perturbations over Moho depth perturbations because we have more picks for first arrivals than for wide-angle reflections, and their uncertainties are much lower. Finally, we set the least-squares tolerance to 1 ms.

Workflow

To obtain a final velocity model, we need to build an initial model in which rays can be traced and synthetic traveltimes calculated for the first modeling iteration. The computed synthetic traveltimes are then compared with the picked traveltimes, and the inversion reduces the misfit between the two sets of traveltimes by perturbing the initial velocity model. The forward and inverse problems run until the misfit is reduced

to a χ^2 of approximately 1. A χ^2 of 1 is achieved when the synthetic arrival times are in agreement with the picked arrival times, within their uncertainty range (Bevington, 1969). When the acceptable final model is reached, model resolution and model uncertainties are evaluated using checkerboard tests, restoration resolution tests, and Monte Carlo analysis. We then repeat this workflow while decimating the number of OBSs used to investigate the relationship among the instrument spacing, data resolving power, and the produced velocity model uncertainty.

Input velocity model

Because the principle of linearized tomography inversion is based on perturbing a starting velocity model, we first built an input velocity model using preexisting velocity information across the Orphan Basin (Figure 4a). The input model must be smooth (no velocity jump) and as simple as possible. A smoothed average vertical velocity profile in the crust and an average Moho depth along the central part of the Lithoprobe 86-6/86-8 line (Chian et al., 2001) are used for the initial velocity structure of the western part of the model. For the easternmost part, we use a smoothed vertical velocity profile in the crust and the Moho depth on the FLAME line (Gerlings et al., 2011) at its crossing with the OBWAVE line. The Lithoprobe 86-6/86-8 line and the FLAME line are wide-angle reflection and refraction profiles with improved structural constraints from coincident seismic reflection lines. Velocities are set to 7.5 km/s at the Moho, and they linearly increase from 7.5 to 8.5 km/s, at the base of the model. Vertical velocity structures and Moho depths are very different between the western and the

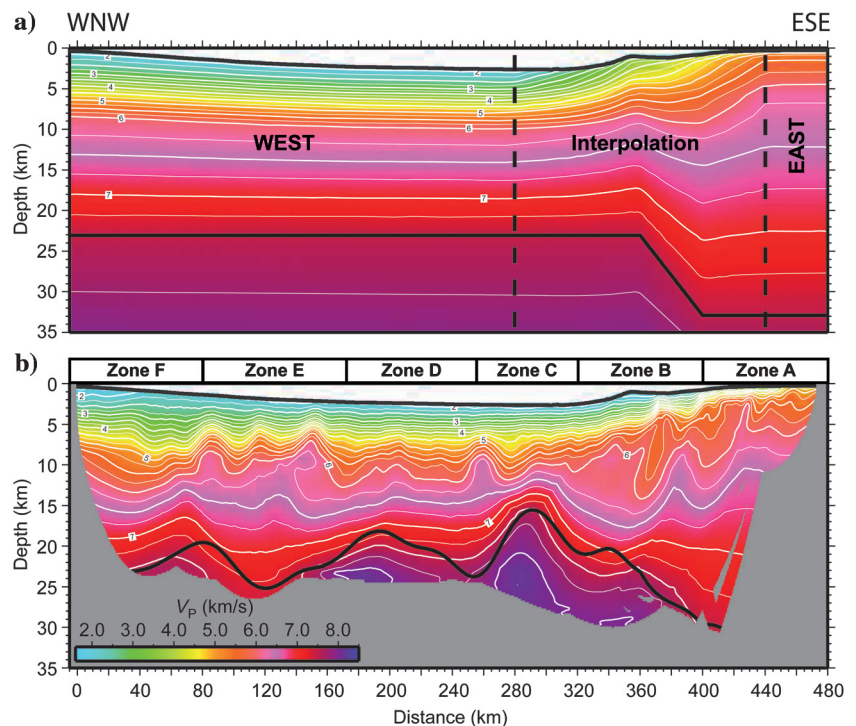


Figure 4. (a) Input velocity model. Within the dashed lines, velocities are linearly interpolated between the eastern and the western regions. White contours are shown every 0.25 km/s and annotated every km/s. (b) Final velocity model computed after five iterations. The model is masked (gray) where there are no rays to define the velocities or the Moho depth. Zones A to F are described in the subsection “Interpretation of the model.”

eastern parts of the model because the western part corresponds to the deep sedimentary basin whereas the eastern part overlies the nearly unstretched continental crust of the Flemish Cap. Thus, we set (1) a sharp variation in Moho depth corresponding to the morphology of the seafloor at distances of 360 to 400 km, and (2) a 160-km-wide interpolation zone, from 280 to 440 km, between the western and eastern parts of the model. In addition, the stability of the inversion was improved using a sharper transition between Moho depths, as given in Figure 4a.

RESULTS

Velocity model

Figure 4b shows the final velocity model obtained after five iterations. The model is shown only over the region with ray coverage. We observe that the model shows a high degree of detail, even though we use minimum a priori information for the input velocity model. A model with minimum structure should have a normalized χ^2 close to one to explain the data without overinterpretation (Bevington, 1969). The normalized χ^2 of the input velocity model is equal to 35.9, with an initial rms arrival time misfit t_{rms} of 472 ms. After five iterations, normalized χ^2 values of the final model reduce to 0.961, 0.954, and 0.960 for the first arrivals, the P_mP arrivals, and all the picked arrivals, respectively. The similarity of the χ^2 values indicates that refracted first arrivals and later

P_mP reflected arrivals are taken into account in a balanced way during the inversion. The final model shows the variations in velocity and Moho depth along the line. The Moho interface defines the base of the crust. Following the interpretation of Chian et al. (2001), we use 5.3 and 6.5 km/s, the velocities at the top of the prerift sediments and at the boundary between the upper and lower crusts, respectively, to define the top of the basement and the middle crust in our model. We observe large variations in depths of the Moho and top of basement (highlighted by the transition from yellow to orange in Figure 4b) along the profile, with shorter wavelength variations characterizing the upper crust and longer wavelength variations in the lower crust. Some particular features are (1) a series of clear basement highs in the western part of the model (distances of 85, 115, and 155 km) and in the eastern part (at distances greater than 310 km), (2) smooth basement and crustal features in the central part of the basin (distances between 160 and 240 km), and (3) a major basin at 270 km that is slightly offset from the major crustal thinning at 280 km.

Traveltime residuals and ray density

The traveltime residuals (Figure 5) give the difference between the picked arrival times and the computed arrival times after ray tracing in the model. The residuals in the initial velocity model mostly fall between ± 1 s, which, in the final model, reduces to ± 0.15 – 0.2 s in agreement with the uncertainty of 200 ms for the P_mP picks.

The derivative weight sum (DWS, Figure 6) is an indication of the ray density near the velocity nodes in the final model (Thurber, 1983). The ray density is best in the upper part of the model and is generally very high in the crust, except on the sides of the model, where rays are traveling in only one direction, and between 80 and 170 km, where the data are noisy and fewer rays are crossing in this area. An alternative explanation is that the nature of the crust in this zone increases the attenuation and/or dissipation of the seismic energy.

Qualitative resolution: Checkerboard tests

A typical way to assess the qualitative resolution of the model derived from traveltime tomography is to use checkerboard tests (e.g., Zelt and Barton, 1998). The diagrams resulting from this analysis show which size of structures we can expect to be resolved in which parts of the model. To perform a checkerboard test, we introduce a $\pm 5\%$ periodic velocity perturbation into the final model and trace the rays in the perturbed model to produce synthetic arrival times. We randomize the synthetic arrival times following Zhang and Toksöz (1998), with one part of the randomization linked to instrumental uncertainties (i.e., relocation and timing uncertainties that are constant for each OBS, with maximum values of ± 62.5 ms) and the other part due to picking uncertainties (values varying for each pick, with a maximum of half the pick uncertainty). Finally, we invert the randomized picks in the original input model. The difference between this inversion result and the final model (Figure 7) shows the wavelength of perturbations that can be recovered across the model. This

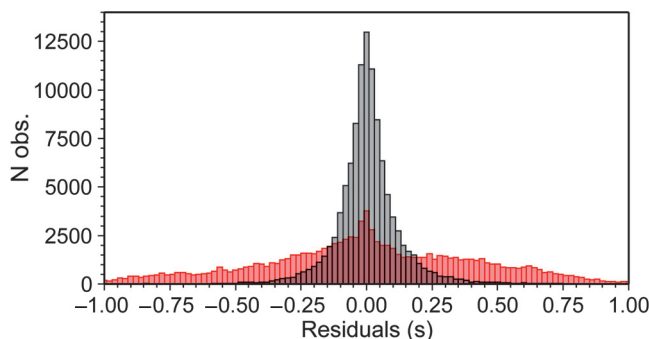


Figure 5. Histograms of the distributions of the traveltime residuals after ray tracing in the initial model (in red) and after the fifth iteration (in black). Bins are 20 ms wide; N obs. refers to the number of observations. Outliers that have a residual time greater than 1 s are not shown.

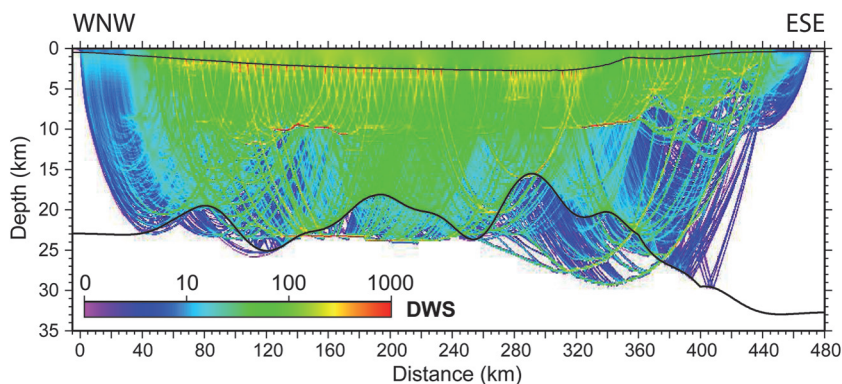


Figure 6. DWS in the final velocity model. Higher values of DWS indicate regions with greater ray coverage and better velocity resolution.

gives insight about the size of the smallest structure that can be imaged with the particular acquisition configuration applied.

Structures that are 25 km wide \times 10 km high are well modeled in the sediments and crust along most of the profile (distances 20–450 km; Figure 7a). However, recovery of the perturbation pattern is of lower quality at both ends of the model, where an insufficient number of crossing rays limits the resolution of the velocities. A structure 25 km wide \times 5 km high is well defined in the sediments and upper crust, especially for distances of 20–320 km (Figure 7b). These perturbations are also recovered in the lower crust for distances of 200–350 km. Because there are few rays in the lower crust

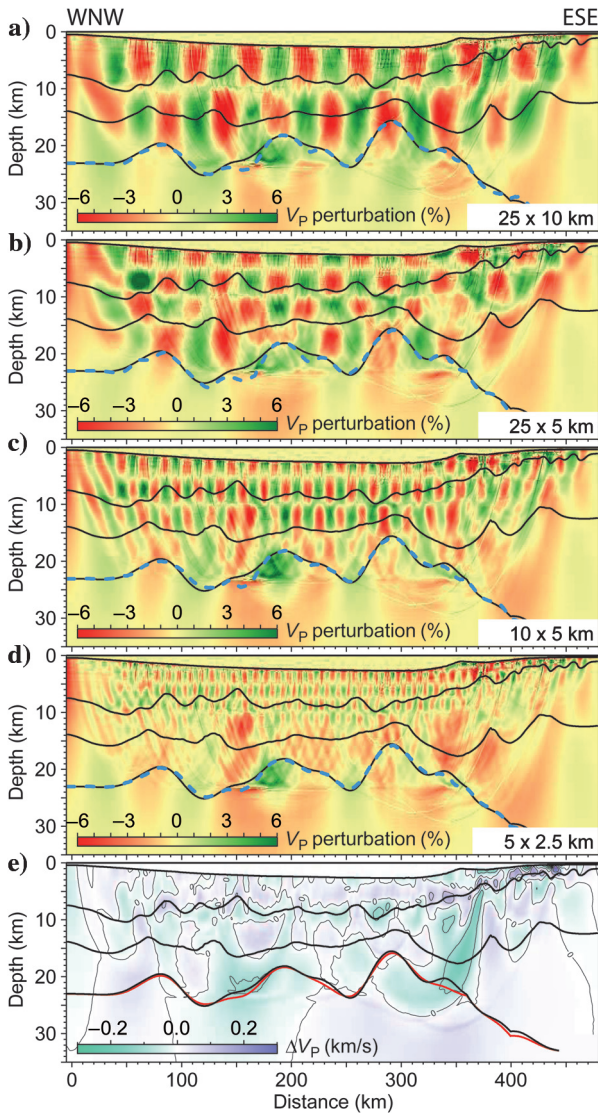


Figure 7. Results of the checkerboard tests for perturbation cells: (a) 25 km wide \times 10 km high, (b) 25 km wide \times 5 km high, (c) 10 km wide \times 5 km high, (d) 5 km wide \times 2.5 km high, and (e) result of the restoration resolution test. The black lines represent the bathymetry, the 5.3 km/s velocity contour for the top of basement, the 6.5 km/s velocity contour for the middle of the crust, and the Moho from the final velocity model (Figure 4). The dashed blue line shows the recovery of the Moho interface that was not perturbed in these tests. The red line shows the Moho recovered after the restoration resolution test.

beneath Flemish Cap, these same structures are not resolved at depths greater than 10 km and distances greater than 350 km. The model is able to define a structure 10 km wide \times 5 km high in the sediments and the upper crust over the entire basin, from a distance 40 to 350 km (Figure 7c). This good resolution disappears progressively beneath the Flemish Cap because there are fewer rays in this area to constrain the calculation. The tomography model is able to define a structure 5 km wide \times 2.5 km high only in the sediments (Figure 7d). We also observe that the cells are not completely recovered at the ends of the profile. This is due to the wave propagation being mainly one directional in these areas. Velocities and Moho depths are not well recovered for model distances of 140 to 195 km and depths greater than 10 km (Figure 7). This is consistent with the low ray density in this area (see Figure 6 and the subsection “Traveltime residuals and ray density”).

The restoration resolution test is used to overcome the limitations of the checkerboard tests that stem from the differences in raypaths computed for the checkerboard tests and the final model (Zhao et al., 1992). The restoration resolution test consists of running the same tomography inversion as before, but using synthetic arrival times calculated from ray tracing in the final velocity model. These arrival times are randomized before the inversion following the same method as for the checkerboard tests. The result from the restoration resolution test and the final model are subtracted for comparison (Figure 7e). We observe a generally good recovery of the original model, with velocity differences less than 100 m/s, except between distances of 340 and 380 km and depths of 5 and 20 km, where many rays travel in only one direction (Figure 6), creating some smearing and thus lower resolution. This is also where the Moho differs the most because velocities here are not resolved as well as in the rest of the model.

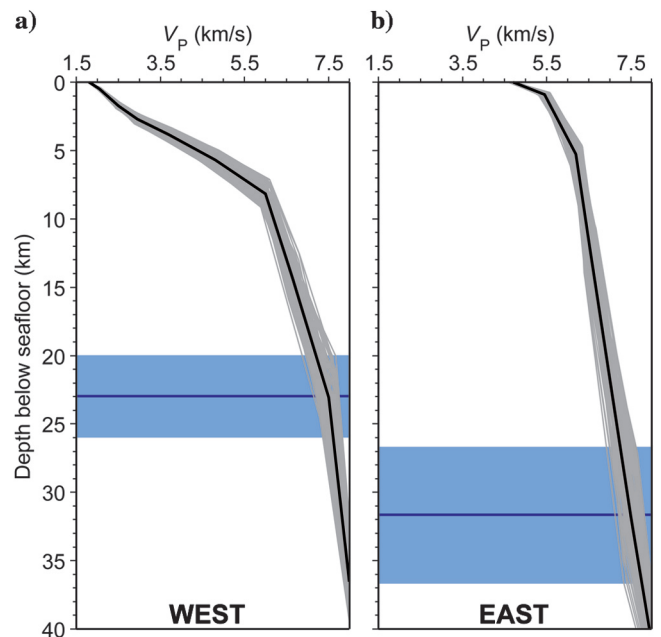


Figure 8. Monte Carlo randomization of the (a) western and (b) eastern parts of the model. The black lines correspond to the original input velocity profiles, gray lines correspond to all randomized velocity profiles, and blue horizontal lines correspond to the original depth of the Moho. The blue areas define the bounds for randomization of the Moho depth. See the text for more details.

Quantitative resolution: Nonlinear Monte Carlo analysis

A nonlinear Monte Carlo analysis allows us to determine the resolution of the model in a more quantitative way. Following the strategy of Korenaga et al. (2000), we randomize the input model to create 100 different input models (Figure 8a–8b). All the parameters used to create the input model presented in Figure 4 are randomized. Thus, we randomize velocities in the crust ($\pm 2.5\%$), depths of the Moho (± 3 km in the western part and ± 5 km in the eastern part), western and eastern boundaries of the interpolation zone (± 20 km), and the distances where we set the inflection points on the Moho (± 10 km). We create 100 sets of randomized arrival times following Zhang and Toksöz (1998), similar to the checkerboard tests (see the subsection “Qualitative resolution: Checkerboard tests”). We run the 100 models using the same parameters as in the final model and produce standard deviations for the P-wave velocities and the Moho depths (Figure 9a) and an average velocity model (Figure 9b). This means that the average model presented in Figure 9b is statistically true within the given range of values presented in Figure 9a.

We observe that the average velocity model resulting from the Monte-Carlo analysis (Figure 8c) is very similar to the final velocity model (Figure 4b). Thus, the result of the modeling is very stable. The standard deviations of velocities are generally less than 50 m/s in most of the crust, and standard deviations of the Moho depths are generally less than 1 km (Figure 9). Greater velocity standard deviations are observed in the part of the crust (model distances of 140 to 180 km and depths greater than 10 km) where poor recovery of the checkerboard patterns is observed. However, standard devia-

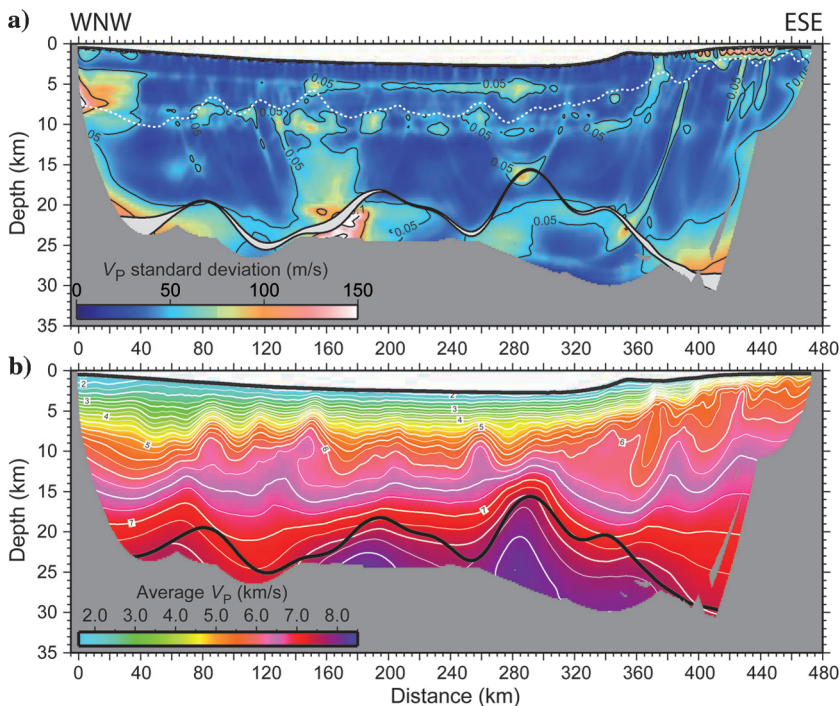


Figure 9. Results of the Monte Carlo analysis. (a) Standard deviations for velocities and depth of the Moho interface. The dotted white line shows the depth of the 5.3 km/s velocity contour of the final velocity model (Figure 4). The gray area shows the average depth of Moho ($\pm 1\sigma$); black contours for velocity deviations are shown every 50 m/s, and (b) average velocity model.

tions in this area of the crust generally do not exceed 75 m/s, which is still very low. Note that this is also the part of the model where the standard deviation of the Moho depth is relatively large (1.5–2 km). For distances less than 50 km, the relatively high standard deviations for velocity (100–150 m/s) are caused by an absence of refracted rays crossing in this part of the model because no instruments were deployed at distances less than 45 km. The standard deviation for the Moho depth in this area is also increased because of the nonuniqueness of the solution of the tomographic inversion because rays do not cross in this area. Similarly, we observe greater standard deviations for lower crustal velocities and for the Moho depth at distances greater than 380 km for the same reasons. Two “stripes” of larger standard deviations are located around 2–3 and 7–9 km below the seafloor, coinciding with the main inflection points in the vertical velocity profiles (Figure 8a). The same pattern also results in the larger standard deviations immediately beneath the seafloor of the Flemish Cap on this side of the line (Figure 8b). Over most of the model, however, the standard deviations of velocities and Moho depths are very low (< 50 m/s for velocities and 1 km for the Moho depths), showing that the model is very robust.

DISCUSSION

Tests with different instrument spacing

Typical survey configuration

To examine the degree to which our reduced OBS spacing has improved model resolution, we calculate the resolution for a more typical survey configuration. Such a configuration consists of a similar shot spacing as in our study (i.e., approximately 150 m) but a much larger OBS spacing (10 to 25 km). To compare our results with a typical configuration, we run a model using picks from every fourth OBS, including the picks added after the coherency filtering. Thus, the spacing of the instruments varies from 12 to 20 km for this “typical spacing” model. After eight iterations using 27,341 picks, normalized χ^2 values of the velocity model reduce to 1.013, 1.063, and 1.024 for the first arrivals, the P_mP arrivals, and all the picked arrivals, respectively.

Figure 10 shows a comparison of results from the Monte-Carlo analysis and checkerboard tests for the OBWAVE and the typical spacing models in the area of the model that includes the denser OBS spacing. The average velocity model with the typical spacing shows fewer details than the OBWAVE model (Figure 10a and 10b). In particular, the shape of the Moho is very different and the high velocities for distances from 270 to 320 km are not recovered with the typical spacing data. This latter result is incongruous with the presence of ultrastretched crust in this area, as observed in the final model (Figure 4). The standard deviations are much larger for the typical spacing model than for the OBWAVE model (Figure 10c and 10d). In particular, standard

deviations for the Moho depth are roughly five times higher in this area of the model with typical spacing compared with the OBWAVE model (i.e., 2.5 versus 0.5 km). Checkerboard tests show poorer recovery of the perturbations for the typical spacing configuration compared with the results for the OBWAVE model (Figure 10e to 10h). In particular, the perturbations are recovered at greater depths and the pattern tends to be clearer for the full OBWAVE model. The restoration resolution tests also show better recovery for the OBWAVE model than for the typical spacing model (Figure 10i and 10j). However, we can observe that the velocity perturbation at depths between 15 and 20 km and distances between 280 and 300 km (the red cell below the Moho interface, Figure 10e and 10f) is better recovered for the typical spacing model than for the OBWAVE model, even though we know that the velocity structure in this area is considerably different than the structure determined with typical spacing. This observation indicates that checkerboard and restoration resolution tests need to be used and interpreted with caution.

Monte Carlo analyses with different configurations

To quantitatively determine the dependence of the resolution of a model to the instrument spacing and instrument position along a

refraction profile, we ran Monte Carlo analyses for instrument decimations of all possible combinations up to five. Thus, in addition to the two Monte Carlo analyses discussed above, we perform 13 extra analyses. The results of the 15 analyses (five configurations with every fifth instrument position, four for every fourth position, three for every third position, second for every second position, and one for single instrument spacing) are compiled in Figure 11. As expected, we observe that using fewer instruments results in (1) increased difference between the model velocity and the full OBWAVE model (Figure 11a and 11b) and (2) increased standard deviations for velocities and depths of the Moho interface (Figure 11c and 11d). However, we also observe significant variations in the dispersion of the results. For example, the rms value for standard deviations of the depth of the Moho interface can be, in particular cases of decimations with one instrument out of three and one instrument out of five, lower than for the full OBWAVE model. This is likely because the Moho interface solutions do not strongly depend on the initial model for these instrument configurations. Indeed, the Moho interface solutions for these instrument configurations are considerably different than for the full OBWAVE model (more than 500 m and 1.2 km average difference for the discussed instrument decimation of 3 and 5, respectively, Figure 11b and 11d).

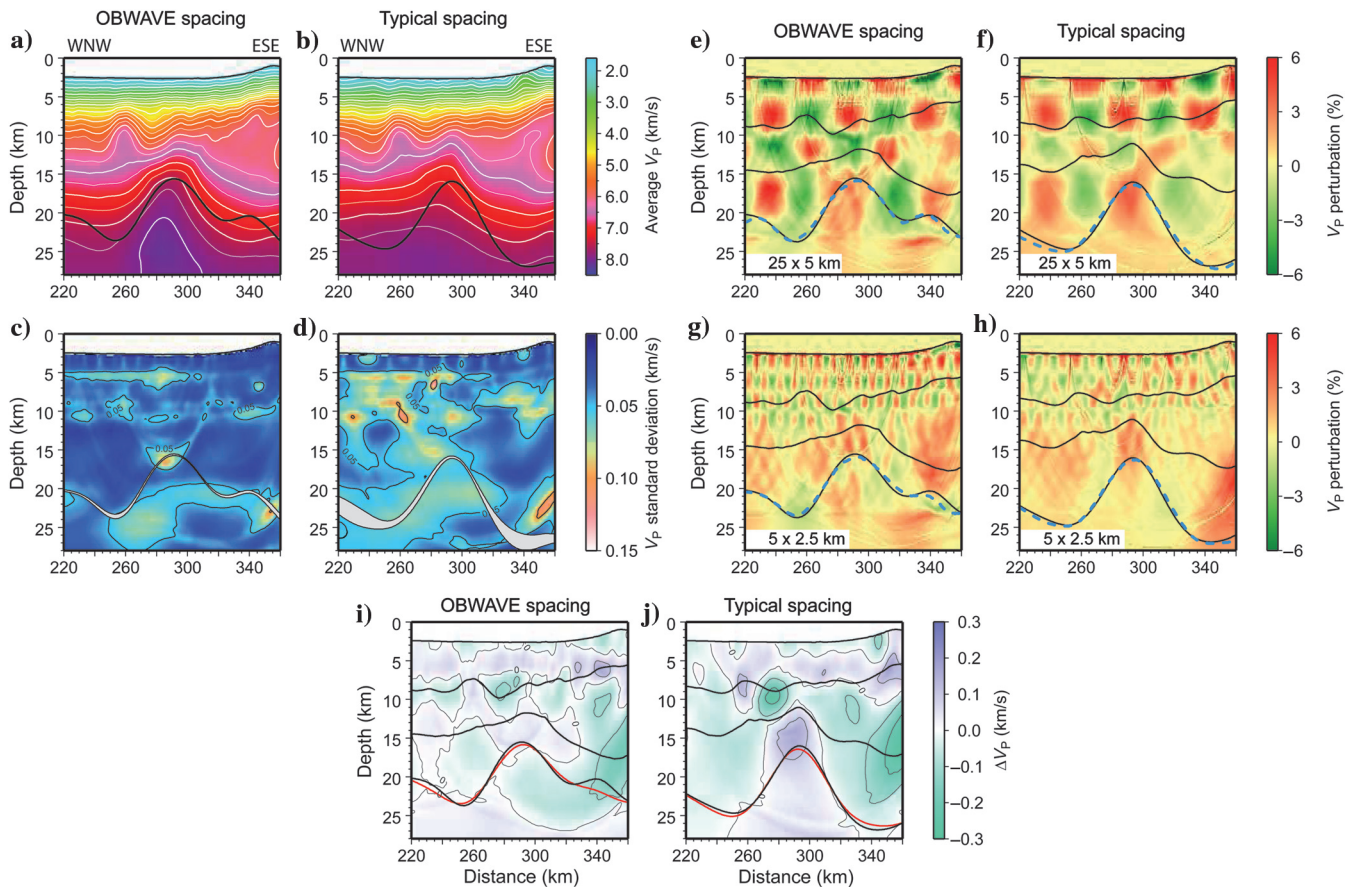


Figure 10. Comparison of the resolution tests at the center of the model between dense OBWAVE instrument spacing (left column) and a typical instrument spacing using every fourth receiver (right column). Results are shown after five iterations for the OBWAVE spacing and eight iterations for a typical spacing. Color scales and lines are the same as in Figures 4, 7, and 9. (a and b) Average velocity models from Monte Carlo analyses. (c and d) Standard deviations resulting from the two Monte Carlo analyses. Results of the checkerboard tests with perturbation cells: (e and f) 25 km wide \times 5 km high and (g and h) 5 km wide \times 2.5 km high. (i and j) Results from the restoration resolution tests.

Moreover, instruments in sparse configurations may, by chance, be at locations in which either high- or low-quality data are recorded, leading to low dependence on the input model.

Furthermore, a Monte Carlo analysis using all the instruments but only every second arrival pick gives almost exactly the same results as the OBWAVE model, including standard deviations (see the blue stars in Figure 11). This observation is critical because typical surveys, including this one, often use 1 min shot interval. For the OBWAVE survey, a 2-min shot interval would have eliminated the problem of the wrap-around noise without affecting the resulting velocity model. Thus, the choice of the instrument and shot spacing is critical depending of the needs of the survey and should be considered relative to expectations of the survey and its cost.

Interpretation of the model

There is good agreement between the OBWAVE velocity structure and the reflection structure imaged along the coincident seismic reflection profile and check-shot data from the Great Barasway borehole, despite this drillhole being some 20 km to the side of the OBWAVE profile (Figure 12). For example, excellent agreement is observed between the tomographic velocities and the faulted blocks delineated by the reflection image (Figure 12b), although the velocity model is smooth. To facilitate discussion of the highly variable structures across the basin, we divide the OBWAVE profile into six zones from east to west (shown in Figures 4b and 12) as follows:

- 1) Zone A: The Flemish Cap section, where the seafloor depth is less than 300 m, the sedimentary cover is very thin, and the upper crust contains offsets in the velocity contours marking the presence of tilted blocks (e.g., following the 6 km/s contour on Figure 4b).
- 2) Zone B: The Flemish Pass section, where crustal thinning of the Flemish Cap becomes more distinct than in zone A. We observe two major tilted blocks with sediment infill that accommodates the main crustal thinning (Figures 4b and 12a).
- 3) Zone C: The East Orphan Trough, where the Moho is shallowest at only 15.5-km depth, the crust is thinnest (less than 7 km), and a deep sedimentary basin is observed immediately to the west. Because the crust is extremely thinned in this area, serpentinization might be expected. However, the data show clear 8 km/s apparent velocities just below the Moho discontinuity, which are characteristic of unaltered mantle peridotites (e.g., Figure 3a; see the first arrivals at offsets $> \sim 75$ km). Furthermore, the seismic reflection profile shows a sharp change in the reflection character across the modeled Moho interface, from the highly reflective lower crust to the highly transparent uppermost mantle (Figure 12c). Thus, in this area, apparent velocities are typical for the unaltered mantle and the seismic reflection profile show low reflectivity, which are strong indications that there is probably very little or no serpentinization of mantle rocks in this area. This is surprising because in other areas of extreme continental extension and mantle exhumation (e.g., the Iberian margin; Manatschal, 2004), the mantle is significantly serpentinized.

- 4) Zone D: The flat area, where the crustal isovelocity contours (5.3 to 7.5 km/s) are for the most part subhorizontal, sediments are thicker and deeper, and basement topography is subdued. In contrast, the Moho crosses the isovelocity contours, suggesting a more complex transition from lower crust to mantle (e.g., Braile and Chiangl, 1986). This is consistent with observations of a complex set of potential “ $P_m P$ -like” phases in this section (Figure 3b). At depths from approximately 8–15 km and distances from approximately 220–260 km, the reflection structure suggests the presence of a deep basin but the isovelocity contours are flat (Figure 12d). In addition to the flat isovelocity lines, the velocities themselves range from approximately 5.3–6.5 km/s, which is unreasonably high for sediments and characteristic of crystalline crust composed of metamorphosed sediments. This strongly suggests that wide-angle refraction data can provide information that is highly complementary to that obtained by seismic reflection imaging, particularly in cases in which the top of the crystalline crust is deep and even the longest seismic reflection streamers do not provide sufficient source-receiver offsets for accurate determination of rock velocities.

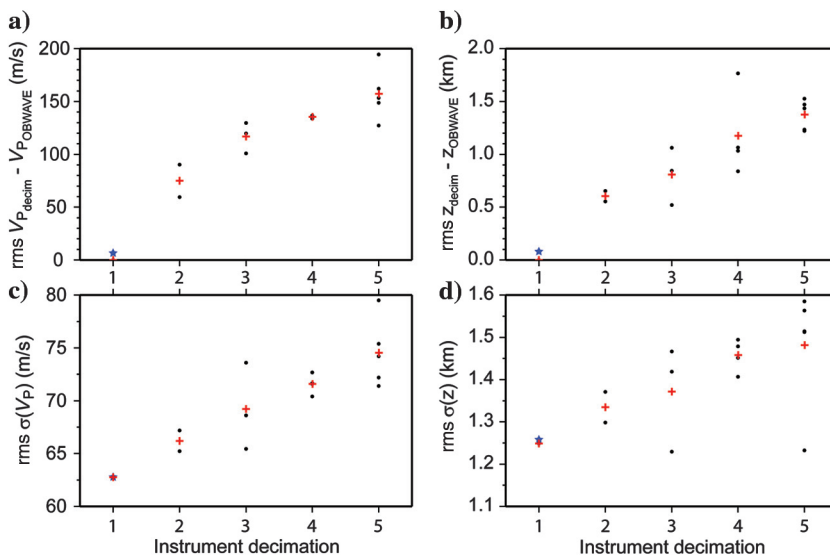


Figure 11. Synthesis of the models obtained after Monte Carlo analyses using all the instruments (instrument decimation = 1) or only part of the instruments (instrument decimation > 1), for each combination. Plots of rms values of (a) the differences of velocities between the average model using part of the instruments ($V_{p,decim}$) and the average model using all the instruments ($V_{p,OBWAVE}$), (b) the differences of Moho depths between the average model using part of the instruments (z_{decim}) and the average model using all the instruments (z_{OBWAVE}), (c) the standard deviation for the velocities, $\sigma(V_p)$, and (d) the standard deviations for the Moho depths $\sigma(z)$. The black dots correspond to actual model results, and the red crosses show the average rms values. The blue stars correspond to the values obtained using one pick out of two in the densest instrument configuration.

- 5) Zone E: The central block, where velocities show the presence of three basement highs (Figure 12b) underlain by a thicker crust (Figure 4b). The structure of the crust in this zone is significantly different than in zone D.
- 6) Zone F: The West Orphan Trough, where we observe a thick sedimentary basin and thinning crust. The age of this westerly trough is not known, and it could be Triassic, Jurassic, and/or early Cretaceous.

Vertical velocity gradients

In an attempt to assess lateral variations in the nature of the crust, we compute and display the vertical velocity gradients along the OBWAVE profile (Figure 13). The tomographic model used for the gradient computation is smooth with no velocity jumps even between the sediments and the basement, where they are known to exist in nature. Thus, the velocity gradient, immediately below the 5.3 km/s contour in Figure 13b, is not real. This apparent high-velocity gradient does not affect the result shown in Figure 13a because the first 2 km below the 5.3 km/s contour in Figure 13b was not taken into account for the computation of the average crustal velocity gradient.

We observe that the plot of the average vertical velocity gradients appears to outline unique crustal zones (Figure 13a). As expected for our smooth tomographic model, the vertical velocity gradients are strongly linked to the amount of crustal thinning: The stronger the thinning, the greater the vertical velocity gradient. Average velocity gradients in the crust reach 0.33 s^{-1} where the crust is the thinnest. However, we also observe that in zones D and E, the crust has a similar thickness although the average vertical velocity gradients are quite different with values of 0.17 s^{-1} (zone D) and 0.1 s^{-1} (zone E). We suspect that this may be due to the contrasting nature of the crust between zones D and E, leading to (1) different deformation styles and (2) the formation of the White Sail Fault separating the western from the eastern Orphan Basin. Furthermore, we observe that ray density is limited in the lower crust in this area (i.e., zone E), in contrast to the rest of the model (Figure 6, and see the subsection “Traveltime residuals and ray density”). This suggests that the crust in zone E might have a different lower crustal composition than the rest of the model, preventing rays from traveling through this region. This might further suggest a thicker/stronger block of continental crust inherited from Avalon crust that is more resistant than the surrounding crustal material. Péron-Pinvidic and Manatschal (2010) interpret this block from profile 86-6/86-8 of Chian et al. (2001) as an H-block (hanging-wall block, defined by Lavier and Manatschal, 2006).

Comparison with Jeanne d’Arc Basin

The Orphan and Jeanne d’Arc Basins are failed rifts with highly stretched continental crust. However, the general crustal structure across the Orphan Basin is quite different than that across the Jeanne d’Arc Basin (Figure 14). The Jeanne d’Arc Basin presents a 100–150-km-wide rift and a 20-km-thick sedimentary basin. The Murre fault, defining the western border of Jeanne d’Arc Basin cuts at least to the middle crust, and the crust is thinned to less than 10 km (de Voogd and Keen, 1987; Keen and Dehler, 1993; Deptuck et al., 2003). In contrast, the Orphan Basin is a 400-km-wide rift with a generally thinner sedimentary cover than that in the Jeanne

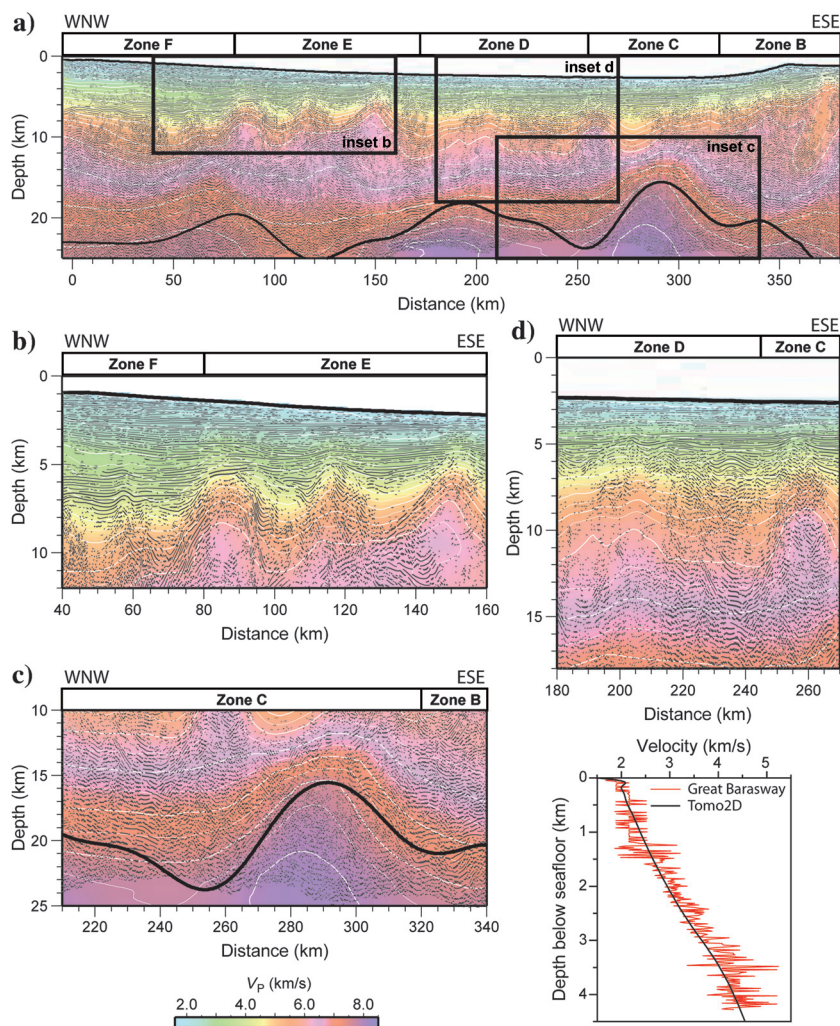


Figure 12. Line drawing of the coincident seismic reflection profile Or0-122 converted to depth using the final tomographic velocity model from this work. Colors and white lines correspond to the OBWAVE velocity model (pastel version of Figure 4b; a color scale is shown at the bottom-left corner of the figure). (a) Image for the part of the model in which there is coincident seismic reflection data. The vertical exaggeration is four. Black rectangles highlight the areas shown in panels (b, c, and d). (b) Zone with basement highs in the western part of the Orphan Basin. The vertical exaggeration is five. (c) Zone where the Moho is the shallowest. The vertical exaggeration is four. (d) Zone where high velocities were not expected because deep reflections on the seismic reflection image outline a possible syn-rift sedimentary basin. The vertical exaggeration is six. Zones B to F are the same as in Figure 4b. (e) Comparison with check-shot data from the Great Barasway borehole (model distance of 173 km).

d’Arc Basin. It is characterized by present-day deep bathymetry (unfilled accommodation) and multiple faults, which terminate into the midcrust.

Although crustal thinning takes place in both basins, we observe that the Moho discontinuity is deeper in the Jeanne d’Arc Basin compared with the Orphan Basin, but that the syn-to-post-rift sedimentary infill is much greater in the Jeanne d’Arc Basin (Figure 14). It would seem that rifting in the Orphan Basin almost reached breakup. As a consequence, the Orphan Basin became much wider than the Jeanne d’Arc Basin as extension progressed to the north (West Orphan Basin) and northeast (East Orphan Basin). The Cum-

berland Belt Transfer Zone acted as a decoupling zone between the two basins during the rifting. Even though the two basins are linked, deformation in the Jeanne d’Arc Basin is primarily fault controlled and spatially restricted whereas deformation in the upper and lower crust in the Orphan Basin was regionally distributed. These differences can mostly be caused by different strain rates (e.g., Buck, 1991) during rifting and/or differences in the structural inheritance in the respective preextension lithospheres (e.g., Keppie and Dallmeyer, 1987).

CONCLUSIONS

The final joint refraction and reflection traveltome tomography model of a dense OBS profile allows us to follow the crustal thinning and variable structures across the Orphan Basin. In particular, we observe (1) a zone of extreme thinning, where the crust is thinner than 7 km and where there is no evidence for upper-mantle serpentinization, (2) basement highs and lows highlighting the blocks that are linked to the crustal thinning, (3) relatively high velocities in a structure interpreted from seismic reflection data as a possible sub-basin, highlighting the importance of refraction and wide-angle reflection data modeling for seismic reflection image interpretation, and (4) a central block, identified as an H-block in the literature, which is thicker compared with the remainder of the basin and probably strongly influenced by structural inheritance. A comparison of crustal structures between the Orphan and Jeanne d’Arc Basins shows that they have different styles of rifting even though they are linked. This suggests the presence of a decoupling zone between the two basins that accommodated the differences of deformation rates and/or structural inheritance in the prifrust crust.

The final velocity model using all the instruments with 3–5 km OBS spacing shows improved resolution compared with a typical survey configuration with one instrument every 10 to 25 km. The standard deviation of velocities in the crust after Monte Carlo analysis (<50 m/s) is lower than determined using the typical instrument spacing and show very little dependence on the initial model. Checkerboard tests generally show better perturbation recoveries when using all the instruments, whereas tests with the typical instrument spacing show that some areas have very good resolution even though the velocity structures are not true, as determined through comparison with the coincident seismic reflection profile. This suggests that the checkerboard tests need be used with caution. A 2-min shot interval is sufficient to image properly the velocities and depths of the Moho, avoiding the problem of wrap-around noise, and it is preferred for most refraction surveys aiming at crustal structures. The choice of instrument spacing is critical depending on the target of the survey. This study points out the need to consider the refraction survey design in terms of the imaging expectations and survey cost.

ACKNOWLEDGMENTS

We thank ExxonMobil through a contract from Esso Exploration, Inc., for primary funding of this project. In particular, we thank G. Karner for his help during the project and for his comments on a previous version of this paper. We thank the officers and crew of the R/V *Strait Explorer* and the technical assistants from McGregor Geoscience Ltd. for their help at sea in sometimes challenging conditions. We thank the Geological Survey of Canada — Atlantic Division (GSCA) for the loan of their OBS and E. Flueh for loan

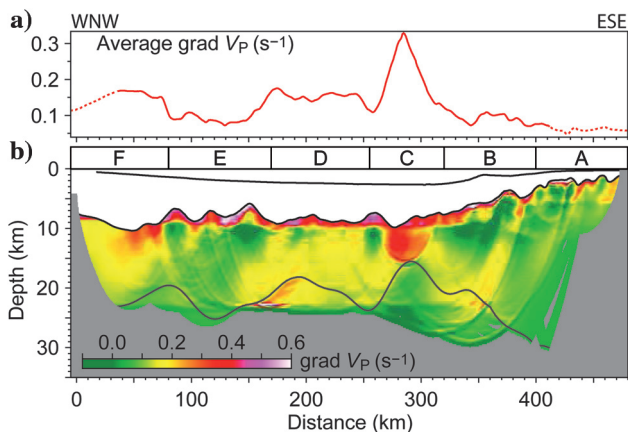


Figure 13. (a) Average vertical velocity gradient from 2 km below the 5.3 km/s velocity contour to the Moho. The curve is dashed where there is no ray coverage across the Moho. (b) Vertical velocity gradients in the crust and upper mantle. Zones A to F are the same as in Figure 4b.

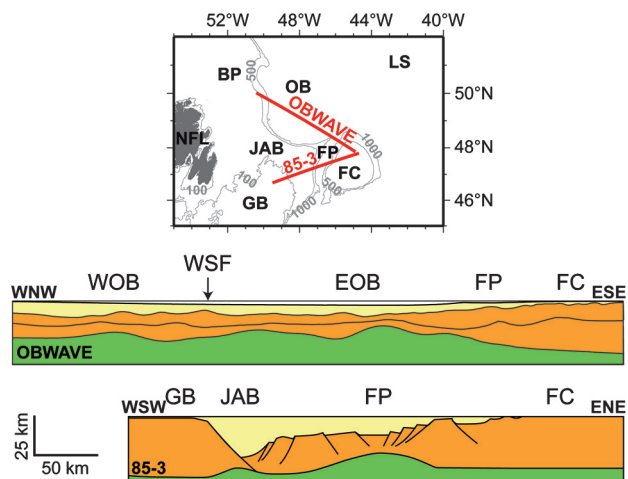


Figure 14. Comparison between the crustal structures along the OBWAVE profile and a line crossing Jeanne d’Arc Basin (crustal structure along Lithoprobe 85-3 from subsidence modeling and seismic interpretation; Keen and Dehler, 1993). The two profiles are shown at the same scale, and their positions are shown on the map on the right. BP, Bonavista Platform; FC, Flemish Cap; FP, Flemish Pass; GB, Grand Banks; JAB, Jeanne d’Arc Basin; LS, Labrador Sea; NFL, Newfoundland; OB, Orphan Basin (EOB, Eastern Orphan Basin; WOB, Western Orphan Basin); and WSF, White Sail Fault.

of IFM-Geomar airguns to help augment the shipboard source array. The OBS data were collected at sea with support from the personnel of the UK-OBIC and from G. Standen, W. Judge, and R. Iuliucci (GSCA and Dalhousie OBS). We thank M. Malinowski, N. Rawlinson, and an anonymous reviewer for their constructive comments. We thank the Canada-Newfoundland and Labrador Offshore Petroleum Board for providing a paper copy of the seismic reflection profile Or0-122 that was used in this work to produce a line drawing for interpretation purposes.

REFERENCES

- Bassi, G., C. E. Keen, and P. Potter, 1993, Contrasting styles of rifting: Models and examples from the eastern Canadian margin: *Tectonics*, **12**, 639–655, doi: [10.1029/93TC00197](https://doi.org/10.1029/93TC00197).
- Baur, F., R. Littke, H. Wielens, C. Lampe, and T. Fuchs, 2010, Basin modeling meets rift analysis — A numerical modeling study from the Jeanne d'Arc basin, offshore Newfoundland, Canada: *Marine and Petroleum Geology*, **27**, 585–599, doi: [10.1016/j.marpetgeo.2009.06.003](https://doi.org/10.1016/j.marpetgeo.2009.06.003).
- Bevington, P. R., 1969, Data reduction and error analysis for the physical sciences: McGraw-Hill.
- Braile, L. W., and C. S. Chiang, 1986, The continental Mohorovičić discontinuity: Results from near-vertical and wide-angle seismic reflection studies, in M. Barazangi, and S. L. Brown, eds., *Reflection seismology: A global perspective*, American Geophysical Union, Geodynamics Series, vol. 13, 257–272.
- Buck, W. R., 1991, Modes of continental lithospheric extension: *Journal of Geophysical Research: Solid Earth*, **96**, 20161–20178, doi: [10.1029/91JB01485](https://doi.org/10.1029/91JB01485).
- Burov, E. B., and M. Diament, 1995, The effective elastic thickness (T_e) of continental lithosphere: What does it really mean?: *Journal of Geophysical Research: Solid Earth*, **100**, 3905–3927, doi: [10.1029/94JB02770](https://doi.org/10.1029/94JB02770).
- Chian, D., I. D. Reid, and H. R. Jackson, 2001, Crustal structure beneath Orphan Basin and implications for nonvolcanic continental rifting: *Journal of Geophysical Research: Solid Earth*, **106**, 10923–10940, doi: [10.1029/2000JB900422](https://doi.org/10.1029/2000JB900422).
- Contrucci, I., L. Matias, M. Moulin, L. Géli, F. Klingelhoefer, H. Nouzé, D. Aslanian, J.-L. Olivet, J.-P. Réhault, and J.-C. Sibuet, 2004, Deep structure of the West African continental margin (Congo, Zaïre, Angola), between 5°S and 8°S, from reflection/refraction seismics and gravity data: *Geophysical Journal International*, **158**, 529–553, doi: [10.1111/j.1365-246X.2004.02303.x](https://doi.org/10.1111/j.1365-246X.2004.02303.x).
- Deptuck, M. E., R. A. MacRae, J. W. Shimeld, G. L. Williams, and R. A. Fensome, 2003, Revised Upper Cretaceous and lower Paleogene lithostratigraphy and depositional history of the Jeanne d'Arc Basin, offshore Newfoundland, Canada: *AAPG Bulletin*, **87**, 1459–1483, doi: [10.1306/050203200178](https://doi.org/10.1306/050203200178).
- De Voogd, B., and C. E. Keen, 1987, Lithoprobe east: Results from reflection profiling of the continental margin: Grand Banks region: *Geophysical Journal International*, **89**, 195–200, doi: [10.1111/j.1365-246X.1987.tb04408.x](https://doi.org/10.1111/j.1365-246X.1987.tb04408.x).
- Enachescu, M., J. Hogg, and K. Meyer, 2004, East Orphan Basin, offshore Newfoundland and Labrador: A deep water super extended rift with potential petroleum system: *Canadian Society of Petroleum Geologists Annual Convention, Expanded Abstracts*.
- Enachescu, M. E., S. Kearsey, V. Hardy, J.-C. Sibuet, J. Hogg, S. Srivastava, A. Fagan, T. Thompson, and R. Ferguson, 2005, Evolution and petroleum potential of Orphan Basin, offshore Newfoundland, and its relation to the movement and rotation of Flemish Cap based on plate kinematics of the North Atlantic: in D. O. Rosen, S. L. Palmes, K. T. Lyons, and G. B. Newton, eds., *Petroleum systems of divergent continental margin basins: 25th Annual Gulf Coast Section SEPM Foundation, F. Bob Perkins Research Conference*, vol. 25, Society for Sedimentary Geology, Gulf Coast Section, 75–131.
- Ford, J. H., and P. F. Johnston, 2003, Biostratigraphic analysis — Texaco Shell et al. BLUE H-28, 2070 to 6103 m: TD: Orphan Basin, East Coast Offshore Newfoundland, Ford Biostratigraphic Services.
- Funck, T., J. R. Hopper, H. C. Larsen, K. E. Loudon, B. E. Tuelholke, and W. S. Holbrook, 2003, Crustal structure of the ocean-continent transition at Flemish Cap: Seismic refraction results: *Journal of Geophysical Research: Solid Earth*, **108**, doi: [10.1029/2003JB002434](https://doi.org/10.1029/2003JB002434).
- Funck, T., H. R. Jackson, K. E. Loudon, S. A. Dehler, and Y. Wu, 2004, Crustal structure of the northern Nova Scotia rifted continental margin (eastern Canada): *Journal of Geophysical Research: Solid Earth*, **109**, doi: [10.1029/2004JB003008](https://doi.org/10.1029/2004JB003008).
- Gerlings, J., K. E. Loudon, and H. R. Jackson, 2011, Crustal structure of the Flemish Cap Continental Margin (eastern Canada): An analysis of a seismic refraction profile: *Geophysical Journal International*, **185**, 30–48, doi: [10.1111/j.1365-246X.2011.04931.x](https://doi.org/10.1111/j.1365-246X.2011.04931.x).
- Huismans, R., and C. Beaumont, 2011, Depth-dependent extension, two-stage breakup and cratonic underplating at rifted margins: *Nature*, **473**, 74–78, doi: [10.1038/nature09988](https://doi.org/10.1038/nature09988).
- Karner, G. D., N. W. Driscoll, and J. K. Weisell, 1993, Response of the lithosphere to in-plane force variations: *Earth and Planetary Science Letters*, **114**, 397–416, doi: [10.1016/0012-821X\(93\)90072-H](https://doi.org/10.1016/0012-821X(93)90072-H).
- Keen, C. E., and S. A. Dehler, 1993, Stretching and subsidence: Rifting of conjugate margins in the North Atlantic region: *Tectonics*, **12**, 1209–1229, doi: [10.1029/93TC00915](https://doi.org/10.1029/93TC00915).
- Keppie, J. D., and R. D. Dallmeyer, 1987, Dating transcurrent terrane accretion: An example from the Meguma and Avalon composite terranes in the northern Appalachians: *Tectonics*, **6**, 831–847, doi: [10.1029/TC006i006p00831](https://doi.org/10.1029/TC006i006p00831).
- Klingelhoefer, F., C. Labails, E. Cosquer, S. Rouzo, L. Géli, D. Aslanian, J.-L. Olivet, M. Sahabi, H. Nouzé, and P. Unternehr, 2009, Crustal structure of the SW-Moroccan margin from wide-angle and reflection seismic data (the DAKHLA experiment) — Part A: Wide-angle seismic models: *Tectonophysics*, **468**, 63–82, doi: [10.1016/j.tecto.2008.07.022](https://doi.org/10.1016/j.tecto.2008.07.022).
- Korenaga, J., W. S. Holbrook, G. M. Kent, P. B. Kelemen, R. S. Detrick, H. C. Larsen, J. R. Hopper, and T. Dahl-Jensen, 2000, Crustal structure of the southeast Greenland margin from joint refraction and reflection seismic tomography: *Journal of Geophysical Research: Solid Earth*, **105**, 21591–21614, doi: [10.1029/2000JB900188](https://doi.org/10.1029/2000JB900188).
- Kusznir, N. J., and R. G. Park, 1987, The extensional strength of the continental lithosphere: Its dependence on geothermal gradient, and crustal composition and thickness: *Geological Society of London, Special Publications*, **28**, 35–52, doi: [10.1144/GSL.SP.1987.028.01.04](https://doi.org/10.1144/GSL.SP.1987.028.01.04).
- Lavier, L. L., and G. Manatschal, 2006, A mechanism to thin the continental lithosphere at magma-poor margins: *Nature*, **440**, 324–328, doi: [10.1038/nature04608](https://doi.org/10.1038/nature04608).
- Lundin, E. R., and A. G. Doré, 2011, Hyperextension, serpentinization, and weakening: A new paradigm for rifted margin compressional deformation: *Geology*, **39**, 347–350, doi: [10.1130/G31499.1](https://doi.org/10.1130/G31499.1).
- Manatschal, G., 2004, New models for evolution of magma-poor rifted margins based on a review of data and concepts from West Iberia and the Alps: *International Journal of Earth Sciences*, **93**, 432–466, doi: [10.1007/s00531-004-0394-7](https://doi.org/10.1007/s00531-004-0394-7).
- McKenzie, D., 1978, Some remarks on the development of sedimentary basins: *Earth and Planetary Science Letters*, **40**, 25–32, doi: [10.1016/0012-821X\(78\)90071-7](https://doi.org/10.1016/0012-821X(78)90071-7).
- Moser, T. J., 1991, Shortest path calculation of seismic rays: *Geophysics*, **56**, 59–67, doi: [10.1190/1.1442958](https://doi.org/10.1190/1.1442958).
- Moser, T. J., T. Eck, and G. Nolet, 1992, Hypocenter determination in strongly heterogeneous earth models using the shortest path method: *Journal of Geophysical Research: Solid Earth*, **97**, 6563–6572, doi: [10.1190/1.1442958](https://doi.org/10.1190/1.1442958).
- Müller, R. D., W. R. Roest, J. Y. Royer, L. M. Gahagan, and J. G. Sclater, 1997, Digital isochrons of the world's ocean floor: *Journal of Geophysical Research: Solid Earth*, **102**, 3211–3214, doi: [10.1029/96JB01781](https://doi.org/10.1029/96JB01781).
- Papazachos, C., and G. Nolet, 1997, P and S deep velocity structure of the Hellenic area obtained by robust nonlinear inversion of travel times: *Journal of Geophysical Research: Solid Earth*, **102**, 8349–8367, doi: [10.1029/96JB03730](https://doi.org/10.1029/96JB03730).
- Péron-Pinvidic, G., and G. Manatschal, 2010, From microcontinents to extensional allochthons: Witnesses of how continents rift and break apart?: *Petroleum Geoscience*, **16**, 189–197, doi: [10.1144/1354-079309-903](https://doi.org/10.1144/1354-079309-903).
- Petit, C., and J. Déverchère, 2006, Structure and evolution of the Baikal rift: A synthesis: *Geochemistry, Geophysics, Geosystems*, **7**, Q11016, doi: [10.1029/2006GC001265](https://doi.org/10.1029/2006GC001265).
- Reston, T. J., 2009, The extension discrepancy and syn-rift subsidence deficit at rifted margins: *Petroleum Geoscience*, **15**, 217–237, doi: [10.1144/1354-079309-845](https://doi.org/10.1144/1354-079309-845).
- Ryan, W. B., S. M. Carbotte, J. O. Coplan, S. O'Hara, A. Melkonian, R. Arko, R. A. Weissel, V. Ferrini, A. Goodwillie, F. Nitsche, J. Bonczkowski, and R. Zensky, 2009, Global multi-resolution topography synthesis: *Geochemistry, Geophysics, Geosystems*, **10**, Q03014, doi: [10.1029/2008GC002332](https://doi.org/10.1029/2008GC002332).
- Sibuet, J. C., S. P. Srivastava, M. Enachescu, and G. D. Karner, 2007, Early Cretaceous motion of Flemish Cap with respect to North America: Implications on the formation of Orphan Basin and SE Flemish Cap–Galicia Bank conjugate margins: *Geological Society of London, Special Publications*, **282**, 63–76, doi: [10.1144/SP282.4](https://doi.org/10.1144/SP282.4).
- Skogseid, J., 2010, The Orphan Basin — A key to understanding the kinematic linkage between North and NE Atlantic Mesozoic rifting: *Central and North Atlantic Conjugate Margins Conference*.
- Stockwell, J. W., 1999, The CWP/SU: Seismic Un*x package: *Computers & Geosciences*, **25**, 415–419, doi: [10.1016/S0098-3004\(98\)00145-9](https://doi.org/10.1016/S0098-3004(98)00145-9).
- Thurber, C. H., 1983, Earthquake locations and three-dimensional crustal structure in the Coyote Lake area, central California: *Journal of Geophysical Research: Solid Earth*, **88**, 8226–8236, doi: [10.1029/JB088iB10p08226](https://doi.org/10.1029/JB088iB10p08226).

- Thybo, H., and C. A. Nielsen, 2009, Magma-compensated crustal thinning in continental rift zones: *Nature*, **457**, 873–876, doi: [10.1038/nature07688](https://doi.org/10.1038/nature07688).
- Van Avendonk, H. J., A. J. Harding, J. A. Orcutt, and J. S. McClain, 1998, A two-dimensional tomographic study of the Clipperton transform fault: *Journal of Geophysical Research: Solid Earth*, **103**, 17885–17899, doi: [10.1029/98JB00904](https://doi.org/10.1029/98JB00904).
- Welford, J. K., and J. Hall, 2007, Crustal structure of the Newfoundland rifted continental margin from constrained 3-D gravity inversion: *Geophysical Journal International*, **171**, 890–908, doi: [10.1111/j.1365-246X.2007.03549.x](https://doi.org/10.1111/j.1365-246X.2007.03549.x).
- Wessel, P., and W. H. Smith, 1998, New, improved version of generic mapping tools released: *Eos — Transactions of the American Geophysical Union*, **79**, 579–579, doi: [10.1029/98EO00426](https://doi.org/10.1029/98EO00426).
- Zelt, C. A., and P. J. Barton, 1998, Three-dimensional seismic refraction tomography: A comparison of two methods applied to data from the Faeroe Basin: *Journal of Geophysical Research: Solid Earth*, **103**, 7187–7210, doi: [10.1029/97JB03536](https://doi.org/10.1029/97JB03536).
- Zelt, C. A., and D. A. Forsyth, 1994, Modeling wide-angle seismic data for crustal structure: Southeastern Grenville Province: *Journal of Geophysical Research: Solid Earth*, **99**, 11687–11704, doi: [10.1029/93JB02764](https://doi.org/10.1029/93JB02764).
- Zhang, J., and M. N. Toksöz, 1998, Nonlinear refraction traveltimes tomography: *Geophysics*, **63**, 1726–1737, doi: [10.1190/1.1444468](https://doi.org/10.1190/1.1444468).
- Zhao, D., A. Hasegawa, and S. Horiuchi, 1992, Tomographic imaging of P and S wave velocity structure beneath northeastern Japan: *Journal of Geophysical Research: Solid Earth*, **97**, 19909–19928, doi: [10.1029/92JB00603](https://doi.org/10.1029/92JB00603).